



## Modeling of a 5 kW<sub>e</sub> tubular solid oxide fuel cell based system operating on desulfurized JP-8 fuel for auxiliary and mobile power applications

Tanvir Tanim\*, David J. Bayless<sup>1</sup>, Jason P. Trembly<sup>2</sup>

Department of Mechanical Engineering, Ohio University, Athens, OH 45701, USA

### HIGHLIGHTS

- Modeling of JP-8 fuel reformer integrated with a tubular solid oxide fuel cell (SOFC) stack.
- Autothermal reformer (ATR) is characterized to obtain optimum performance.
- System does not require external energy and steam at steady state.
- System efficiencies of 39.5% and 32.6% observed at ATR temperatures of 700 °C and 850 °C, respectively.
- Optimum operating range suggested by conducting parametric analyses.

### ARTICLE INFO

#### Article history:

Received 23 May 2012

Received in revised form

7 August 2012

Accepted 9 August 2012

Available online 23 August 2012

#### Keywords:

Autothermal reformer

Solid oxide fuel cell

JP-8 fuel

Auxiliary power unit

Mobile electric power

### ABSTRACT

An onboard autothermal reformer (ATR) integrated with a SOFC stack offers potential for high energy efficiency and utilization, low emission and quiet operation avoiding cost associated with hydrogen storage and infrastructure. Such a system can be a viable and attractive option especially for military's need for quiet and less pollutant Auxiliary Power Unit (APU) and Mobile Electric Power (MEP) units in temporary and permanent base camps [1,2]. A 5 kW<sub>e</sub> Solid Oxide Fuel Cell (SOFC) system operating on desulfurized JP-8 fuel was modeled using Aspen Plus process simulation software to examine the effects of oxygen to carbon ratio (O<sub>2</sub>/C) and steam to carbon ratio (H<sub>2</sub>O/C) at different ATR operating temperatures (700–850 °C), while keeping the SOFC stack temperature constant at 910 °C. Anode recycle steam and heat have been used to reform the desulfurized JP-8 fuel which would make the system lighter and compact for mobile application. The system modeling revealed a maximum net AC efficiency of 39.5% at 700 °C and a minimum of 32.6% at 850 °C ATR operating temperatures, respectively. Sensitivity analysis with respect to fuel utilization factor ( $U_f$ ) and current density ( $j$ ) were also conducted to identify the optimum operating window.

© 2012 Elsevier B.V. All rights reserved.

### 1. Introduction

Solid oxide fuel cells (SOFC) are high efficiency, low emission, solid state, and quiet energy conversion devices. But commercial applications are still limited due to the availability of fuel such as hydrogen (H<sub>2</sub>) and high initial cost. Integrating a hydrocarbon fuel reformer with the SOFC system can minimize the costs and problems associated with hydrogen storage and delivery. The United States Army is interested in developing a fuel cell based portable

power system to support their energy intensive devices. "Silent Watch", Army's term for very deployable power systems with low acoustic and stringent infrared signature levels, make it impossible to use the conventional diesel engines due to the loud noise in some critical operations [1]. Moreover, the large array of communication and situational awareness electronics used in fields cannot be supported by only batteries, for long durations, making this need for power more acute [1]. These types of systems also have high potential to provide power in the temporary and permanent military base camps as a MEP source to provide power for mobile kitchen units, laundry units, heating and refrigeration units, well kit, printing plant, hospital maintenance, bakery plant, water purification, in addition to support the combat, communication and missile systems [2]. As JP-8/jet fuel is the main logistical fuel of the U.S. Army, an APU combined with JP-8 fuel processor can provide a viable power option. It can also be modified and run on diesel fuel

\* Corresponding author. Present address: 127 Reber building, University Park, PA 16802, USA. Tel.: +1 740 447 3560.

E-mail addresses: [tt131309@ohio.edu](mailto:tt131309@ohio.edu) (T. Tanim), [bayless@ohio.edu](mailto:bayless@ohio.edu) (D.J. Bayless), [trembly@ohio.edu](mailto:trembly@ohio.edu) (J.P. Trembly).

<sup>1</sup> Tel.: +1 740 331 4436; fax: +1 740 593 0476.

<sup>2</sup> Tel.: +1 740 331 4921; fax: +1 740 593 0476.

<b>Nomenclature</b>	
<i>Roman letters</i>	
$A, B$	constants in Eqs. (17) and (18)
$D$	diameter of SOFC cell, m
$D_{ik}$	binary diffusion coefficient of species $i$ and $k$ , $\text{m}^2 \text{s}^{-1}$
$D_{K,i}$	Knudsen diffusion coefficient, $\text{m}^2 \text{s}^{-1}$
$D_{i(\text{eff})}$	effective diffusion coefficient of species $I$ , $\text{m}^2 \text{s}^{-1}$
$E$	activation energy, $\text{J mol}^{-1}$
$F$	Faraday constant, $\text{C mol}^{-1}$
$I$	current, A
$j$	current density, $\text{A m}^{-2}$
$K$	Pre-exponential factor, $\text{A m}^{-2}$
$l$	component thickness, m
LHV	lower heating value of fuel, $\text{J mol}^{-1}$
$M_i$	molecular weight of gaseous components $i$ , $\text{kg kmol}^{-1}$
$n$	molar flow rate, $\text{mol min}^{-1}$
$\dot{n}_{\text{fuel}}$	molar flow rate of fuel, $\text{mol min}^{-1}$
$P$	pressure, bar
$P_i$	partial pressure of gaseous components $i$ , bar
$P_{\text{SOFC}}$	SOFC operating pressure, Pa
$P_{\text{el,DC}}$	DC power, W
$P_{\text{el,AC}}$	AC power, W
$P_{\text{comp}}$	compressor power, W
$\bar{r}_p$	mean radius of electrode pore, m
$R_g$	universal gas constant, $8.314 \text{ J mol}^{-1} \text{ K}$
$R_{\text{act}}$	specific resistance, $\Omega \text{ m}^2$
$T_{\text{avg}}$	average temperature, K
$T_{\text{op}}$	SOFC operating temperature, K
$U_f$	fuel utilization
$V$	voltage, V
$V_N$	Nernst voltage, V
<i>Greek letters</i>	
$\Delta \bar{g}_f$	molar Gibbs Free energy of formation, $\text{J mol}^{-1}$
$\delta_{O_2}$	constants in Eqs. (24) and (25)
$\epsilon$	electrode porosity
$\eta_{\text{act}}$	activation polarization, V
$\eta_{\text{con}}$	concentration polarization, V
$\eta_{\text{el,gross}}$	gross AC electric power, W
$\eta_{\text{el,net}}$	net AC electric power, W
$\eta_{\text{ohm}}$	ohmic polarization, V
$v$	fuller diffusion volume
$\xi$	electrode tortuosity
$\rho$	resistivity, $\Omega \text{ m}$
<i>Subscripts</i>	
$a$	anode
$\text{ac}$	activation
$c$	cathode
$\text{con}$	concentration
$e$	electrolyte
$\text{eff}$	effective
$\text{eq}$	equivalent
$i$	gaseous component
$\text{int}$	interconnector
$k$	second gaseous component
$m$	mean
$\text{ohm}$	ohmic
<i>Superscripts</i>	
$a$	anode
$c$	cathode

and eventually integrate in heavy duty trucks, refrigeration units, recreational vehicles (RVs) due to their long inefficient idling operations [3]. It can also be an attractive option for aviation APUs without major modification of the existing fuel system because of lower emission and usability of the exhaust heat to lower the maximum onboard electric load [4].

A number of investigations of SOFC based processes modeled using Aspen Plus has been found in literature using different fuels. Zhang et al. [5] used natural gas in their study. Doherty et al. [6] used two types of biogas to investigate system performance. Biomass-based MW<sub>e</sub> scale combined systems have also been studied comprising of gas turbine and SOFC module to investigate the cycle efficiency and optimum operating range for stationary applications [7–10]. Baratto et al. [11] studied a diesel based APU for commercial heavy duty trucks without recycling of the anode exhaust heat and steam and showed experimental and modeling agreement of results. Roychoudhury et al. [12] investigated a 5 kW<sub>t</sub> JP-8 logistic fuel processor with external steam generator. They mainly focused on the fuel processor and did not include the SOFC stack to understand the overall performance of the system. Therefore, a complete system using a JP-8 fuel based SOFC with APU, which would address the steam management needs and make the best use of exhaust heat, is not available in the literature.

The objective of this study is to evaluate a 5 kW<sub>e</sub> tubular SOFC based system that operates on autothermally reformed desulfurized JP-8 fuel using Aspen Plus process simulation software. The adiabatic ATR was simulated and characterized from 700 °C to 850 °C by varying the H<sub>2</sub>O/C and O<sub>2</sub>/C ratios to obtain optimum H<sub>2</sub>

and CO contents in a non-coking system. A portion of anode exhaust has been mixed with the fresh fuel to provide the steam and heat required for reforming. Finally, parametric analyses were conducted by varying fuel utilization factor ( $U_f$ ) and current density ( $j$ ) to identify the system's performance at different load conditions.

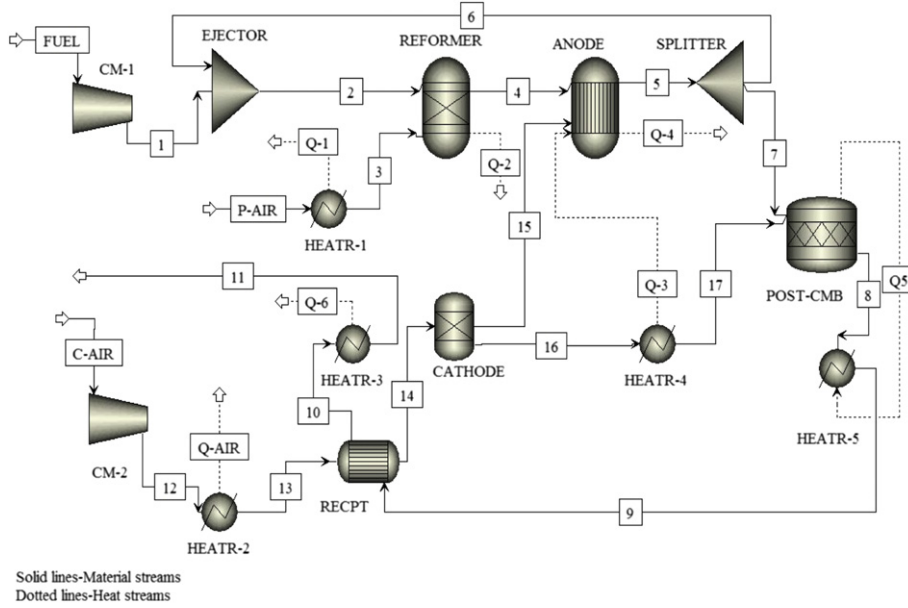
## 2. Model description

### 2.1. Model assumptions

The model is based on zero dimensional approach with steady and isothermal operation. All working fluids are considered as ideal gases neglecting any pressure drop. It is assumed that reforming and shifting reactions reach chemical equilibrium. Only H<sub>2</sub> is assumed to be electrochemically oxidizable, CO is assumed to take part in the water gas shift (WGS) reaction and the lower hydrocarbons (CH<sub>4</sub>, C<sub>2</sub>H<sub>6</sub>, C<sub>3</sub>H<sub>8</sub> etc) are reformed to H<sub>2</sub> [5,6].

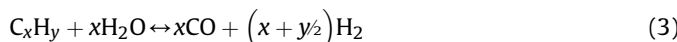
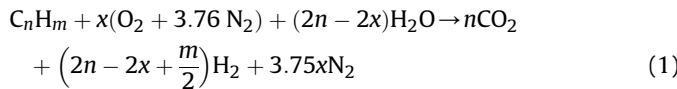
### 2.2. Process flow model

A schematic view of the proposed 5 kW<sub>e</sub> SOFC system is depicted in Fig. 1. The stream named 'FUEL' represents the fresh JP-8 fuel, which is heated to its higher boiling temperature and compressed in the compressor, 'CM-1' block. The discharge pressure of the compressor is set to the pressure ratio:  $P_{\text{fuel}}/P_{\text{SOFC}} = 3.0$  to drive the recirculated anode gas along [5,6,13]. A mixer block named 'EJECTOR' mixes the recirculated anode gas with the fresh fuel. A particular H<sub>2</sub>O/C ratio is manipulated by changing the split

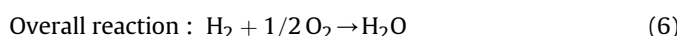
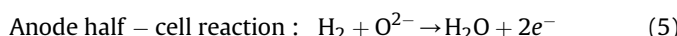
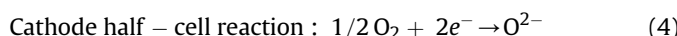
**Fig. 1.** Process flow diagram of the 5 kW<sub>e</sub> SOFC system.

fraction using a Fsplitter module named as, 'SPLITTER'. H<sub>2</sub>O/C ratio is defined as the molar ratio of the number of H<sub>2</sub>O molecules and the combustible C-atoms entering into the 'REFORMER' [13]. H<sub>2</sub>/C and CO/C ratios are defined as the ratio of molar flow rate of H<sub>2</sub> or CO at ATR outlet and inlet streams, respectively. A design specification block is used to maintain the desired H<sub>2</sub>O/C ratio by manipulating the split fraction.

A Gibbs reactor module named 'REFORMER' is used to simulate adiabatic autothermal reforming of JP-8 fuel. A heater module named 'HEATR-1', preheats the air coming into the reformer to supply O<sub>2</sub> flow rate in the reformer to make it adiabatic, to achieve the maximum reformer efficiency [14]. The governing equations of the autothermal reaction, water gas shift (WGS) reaction and steam reforming (SR) reactions are shown in Eqs. (1)–(3), respectively.



The reformed fuel in the ATR outlet mainly contains H<sub>2</sub> and CO gases. Lower hydrocarbons e.g. CH<sub>4</sub>, C<sub>2</sub>H<sub>6</sub>, C<sub>3</sub>H<sub>8</sub> can also be present in the reformed gas and assumed to take part in the internal reforming reactions (Eq. (3)) in the 'ANODE' chamber. The electrochemical reactions are as follows:



As Aspen Plus cannot model the electrochemical reactions shown in Eqs. (4) and (5), the overall reaction (Eq. (6)) is considered instead. The stream 'C-AIR', is compressed in the compressor block

named 'CM-2' and later heated in the heater block 'HEATR-2'. The pre-heated air is further heated in the heat exchanger module (HeatX) named, 'RECPT' by utilizing the hot exhaust gas stream coming out from the post combustor, 'POST-CMB', which simulated by a stoichiometric reactor and 'HEATR-5'. The compressed and heated air (stream '14') goes into the 'CATHODE' block, which is a separator module that separates O<sub>2</sub> from air needed by the electrochemical reaction and consequently simulates the cathode of SOFC. Aspen Plus calculates the flow rate of O<sub>2</sub> based on the equivalent H<sub>2</sub> flow rate at the anode as follow:

$$\begin{aligned} \dot{n}H_{2,\text{eq}} = & \dot{n}H_{2,\text{ATR}} + 1(\dot{n}CO_{\text{ATR}}) + 4(\dot{n}CH_4_{\text{ATR}}) + 7(\dot{n}C_2H_6_{\text{ATR}}) \\ & + 10(\dot{n}C_3H_8_{\text{ATR}}) \end{aligned} \quad (7)$$

Here,  $\dot{n}H_{2,\text{ATR}}$  is the molar flow rate of H<sub>2</sub> contained in the ATR outlet stream, '4'.  $1(\dot{n}CO_{\text{ATR}})$  is the molar flow rate of H<sub>2</sub> that could be produced from CO by the WGS reaction contained in the ATR outlet stream, '4'.  $4(\dot{n}CH_4_{\text{ATR}})$  is the molar flow rate of H<sub>2</sub> that could be produced from 1 mol of CH<sub>4</sub> contained in stream '4' (1 mol of CH<sub>4</sub> produces 3 mol of H<sub>2</sub> and 1 mol of CO that takes part in the WGS reaction and converted to H<sub>2</sub>). The similar statement applies for the higher hydrocarbons e.g.  $\dot{n}C_2H_6_{\text{ATR}}$  and  $\dot{n}C_3H_8_{\text{ATR}}$ .

The amount of H<sub>2</sub> and O<sub>2</sub> consumed in the anode stack is calculated using the known fuel and air utilization factors, respectively in an Aspen Plus calculator block.

$$U_f = \frac{\dot{n}H_{2,\text{consumed}}}{\dot{n}H_{2,\text{eq}}} \quad (8)$$

$$\dot{n}O_{2,\text{consumed}} = 0.5 \cdot \dot{n}H_{2,\text{consumed}} = 0.5 \cdot U_f \cdot \dot{n}H_{2,\text{eq}} \quad (9)$$

$$O_{2,\text{frac}} = \frac{\dot{n}O_{2,\text{consumed}}}{\dot{n}O_{2,\text{in}}} = U_a \quad (10)$$

The calculator block calculates the equivalent H<sub>2</sub> flow rate from Eq. (7). Once the equivalent H<sub>2</sub> flow rate is known the consumed H<sub>2</sub> flow rate can be calculated from Eq. (8). The oxygen flow rate is related to the consumed H<sub>2</sub> flow rate via the overall electrochemical reaction (Eq. (6)) and can be calculated by using Eq. (9).

Aspen Plus calculator block varies the air flow rate to obtain the desired oxygen split fraction which is also equivalent to the known air utilization factor,  $U_a$ . The temperature of the depleted air, stream '16' is raised by using heat liberated from the electrochemical reactions at the heater module named 'HEATR-4'. The stream, '10', still contains substantial amount of heat that is calculated adding another heater module, 'HEATR-3' by setting up the temperature (450 °C) of the final exhaust stream, '11'.

### 2.3. Electrochemical modeling

The cell voltage is calculated by applying the Nernst equation and then subtracting the ohmic, activation, and concentration losses. Average partial pressures have been used in the Nernst equation, given in Eq. (11).

$$V_N = -\frac{\Delta \bar{g}_f}{2F} + \frac{R_g \cdot T_{avg}}{2F} \ln \left( \frac{P_{H_2} \cdot P_{O_2}^{0.5}}{P_{H_2O}} \right) \quad (11)$$

Ohmic losses are calculated by using equations proposed by Song et al. [15] for tubular SOFC. The activation losses are calculated by assuming linear current potential equations for tubular cells [16]. Semi-empirical formulas proposed by Achenbach [17] are used to calculate the exchange current densities for activation voltage loss. Fick's law of diffusion is used to calculate the concentration voltage loss of anode and cathode for tubular cells considering both ordinary and Knudsen diffusion phenomena in the form of effective diffusion coefficient and discussed briefly below. Knudsen diffusion coefficient for straight and round pores [6,16] is given in Eq. (12).

$$D_{K,i} = 97.0 \bar{r}_p \sqrt{T_{top}/M_i} \quad (12)$$

Fuller et al. [18] method is considered to simulate the binary diffusion coefficient

$$D_{ik} = \frac{1 \times 10^{-7} T_{op}^{1.75} \left( 1/M_i + 1/M_k \right)^{1/2}}{P \left( v_i^{1/3} + v_k^{1/3} \right)^2} \quad (13)$$

The effective diffusion coefficient can be calculated from Eq. (14).

$$\frac{1}{D_{i(eff)}} = \frac{\xi}{\epsilon} \left( \frac{1}{D_{K,i}} + \frac{1}{D_{ik}} \right) \quad (14)$$

$$\eta_{con}^c = -\frac{R_g \cdot T_{op}}{4 \cdot F} \ln \left\{ \frac{1 - \left( R_g \cdot \frac{T_{op}}{2} \cdot F \right) \left( \frac{l_a}{D_{a(eff)} \cdot y_{H_2} \cdot P_{SOFC}} \right) \cdot j}{1 + \left( R_g \cdot \frac{T_{op}}{2} \cdot F \right) \left( \frac{l_a}{D_{a(eff)} \cdot y_{H_2O} \cdot P_{SOFC}} \right) \cdot j} \right\} \quad (23)$$

The anode and cathode effective diffusivities are [16] given in Eqs. (15) and (16).

$$D_{a(eff)} = \left( \frac{P_{H_2O}}{P_{SOFC}} \right) \cdot D_{H_2(eff)} + \left( \frac{P_{H_2}}{P_{SOFC}} \right) \cdot D_{H_2O(eff)} \quad (15)$$

$$D_{c(eff)} = D_{O_2(eff)} \quad (16)$$

The polarization losses are modeled using Eqs. (17)–(26).

#### Ohmic loss [15]

$$\eta_{ohm}^a = \frac{j \cdot \rho_a (A \pi \cdot D_m)^2}{8 \cdot l_a} \quad (17)$$

$$\eta_{ohm}^e = \frac{j \cdot \rho_e (B \pi \cdot D_m)^2}{8 \cdot l_c} \cdot A [A + 2(1 - A - B)] \quad (18)$$

$$\eta_{ohm}^e = j \cdot \rho_e \cdot l_e \quad (19)$$

$$\eta_{ohm}^{int} = j \cdot \rho_{int} \cdot (\pi \cdot D_m) \cdot \frac{l_{int}}{w_{int}} \quad (20)$$

#### Activation Loss [16]

$$\frac{1}{R_{act_a}} = \frac{2F}{R_g \cdot T_{op}} \cdot K_{a_{H_2}} \cdot \left( P_{H_2}/P^0 \right)^m \cdot \exp \left( \frac{-E_a}{R_g \cdot T_{op}} \right) \quad (21)$$

$$\frac{1}{R_{act_c}} = \frac{4F}{R_g \cdot T_{op}} \cdot K_c \cdot \left( P_{O_2}/P^0 \right)^m \cdot \exp \left( \frac{-E_c}{R_g \cdot T_{op}} \right) \quad (22)$$

#### Concentration polarization [6,16]

$$\eta_{con}^c = -\frac{R_g \cdot T_{op}}{4 \cdot F} \ln \left\{ \frac{\left( \frac{P_{SOFC}}{\delta_{O_2}} \right) - \left[ \left( \frac{P_{SOFC}}{\delta_{O_2}} \right) - y_{O_2} \cdot P_{SOFC} \right] \exp \left[ \left( \frac{R_g \cdot T_{op}}{4 \cdot F} \right) \left( \frac{\delta_{O_2} \cdot l_c}{D_{a(eff)} \cdot P_{SOFC}} \right) \cdot j \right]}{y_{O_2} \cdot P_{SOFC}} \right\} \quad (24)$$

$$\delta_{O_2} = \frac{D_{K,O_2(eff)}}{D_{K,O_2(eff)} + D_{O_2-N_2(eff)}} \quad (25)$$

Finally, the actual operating voltage of a cell,

$$V = V_N - (\eta_{ohm} + \eta_{act} + \eta_{con}) \quad (26)$$

An Aspen Plus design specification block determines the input fuel flow rate required to achieve the desired DC power ( $P_{el,DC} = VI$ )

**Table 1**  
Composition of JP-8 surrogate fuel [19].

Name	Molecular formula	Weight (%)	LHV (kJ mol <sup>-1</sup> )
Iso-octane	C <sub>8</sub> H <sub>18</sub>	3.66	5064.31
n-Decane	C <sub>10</sub> H <sub>22</sub>	16.08	6293.01
n-Dodecane	C <sub>12</sub> H <sub>26</sub>	22.54	7512.24
n-Tetradecane	C <sub>14</sub> H <sub>30</sub>	16.87	8731.15
n-Hexadecane	C <sub>16</sub> H <sub>34</sub>	12.22	9949.55
Methylcyclohexane	C <sub>7</sub> H <sub>14</sub>	3.51	4256.33
Cyclooctane	C <sub>8</sub> H <sub>16</sub>	4.54	4912.24
n-Butylbenzene	C <sub>10</sub> H <sub>14</sub>	4.72	5563.34
1,2,3,4-tetramethylbenzene	C <sub>10</sub> H <sub>14</sub>	4.28	5505.35
m-Xylene	C <sub>8</sub> H <sub>10</sub>	3.95	4330.97
Teralin	C <sub>10</sub> H <sub>12</sub>	4.14	5356.48
1-Methylnaphthalene	C <sub>11</sub> H <sub>10</sub>	3.49	5594.73

while calculating the voltage loss simultaneously. For current density sensitivity analysis a calculator block determines the input fuel flow rate based on required current,  $I$  using Eq. (27)

$$\dot{n}_{H_2,eq} = \frac{60 \cdot I}{2FU_f} \quad (27)$$

The gross and net efficiencies of the system can be calculated from Eqs. (28) and (29), respectively.

$$\eta_{el,gross} = \frac{P_{el,AC}}{\dot{n}_{fuel} \cdot LHV_{fuel}} \quad (28)$$

$$\eta_{el,net} = \frac{P_{el,AC} - P_{comp}}{\dot{n}_{fuel} \cdot LHV_{fuel}} \quad (29)$$

The composition of JP-8 surrogate fuel used in this study is shown in Table 1.

### 3. Model validation

The ATR module was individually validated against experimental data published by Liu et al. [20] of a kW scale catalytic ATR using hexadecane and dodecane as a diesel surrogate fuel. The simulation result matched more closely with the experimental results at higher O<sub>2</sub>/C ratios shown in Fig. 2. Less fuel reforming is likely to occur at lower O<sub>2</sub>/C ratio, resulting in insufficient heat to promote the steam reforming reactions, which may be the reason for this difference at lower O<sub>2</sub>/C ratios.

To validate the tubular SOFC module in this study a Siemens Power Generation Inc (SPGI) 100 kW natural gas fueled cogeneration system was selected. The 100 kW SPGI system is the world's longest operational SOFC generator with more than 36,900 h (updated on June 2007) of operation [21]. This model is selected as

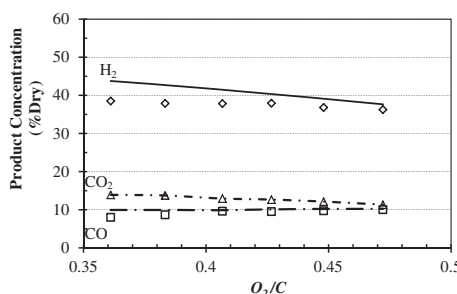


**Fig. 2.** Comparison of experimental (symbols) reformate concentrations [20] with Aspen Plus simulation (lines) for dodecane at H<sub>2</sub>O/C = 2.0 with varying O<sub>2</sub>/C.

**Table 2**  
Model input parameters.

Geometry [6,22,23]	
Cell Length/diameter (m)	1.5/0.022
Anode thickness, $l_a$ (m)	0.0001
Cathode thickness, $l_c$ (m)	0.0022
Electrolyte thickness, $l_e$ (m)	0.00004
Interconnect thickness, $l_{int}$ (m)	0.000085
Interconnect width, $l_{int}$ (m)	0.009
Material Properties [22,24]	
Anode resistivity, $\rho_A$ ( $\Omega$ m)	$2.98 \times 10^{-5} \exp(-1392/T_{op})$
Cathode resistivity, $\rho_C$ ( $\Omega$ m)	$8.114 \times 10^{-5} \exp(600/T_{op})$
Electrolyte resistivity, $\rho_e$ ( $\Omega$ m)	$2.94 \times 10^{-5} \exp(10,350/T_{op})$
Interconnect resistivity, $\rho_{int}$ ( $\Omega$ m)	0.025
Ohmic Loss [15]	
A/B	0.804/0.13
Activation Loss [17,25]	
Pre-exponential factor, $K_a/K_c$ ( $A\text{ m}^{-2}$ )	$2.13 \times 10^8/1.49 \times 10^{10}$
Slope, $m$	0.25
Activation energy, $E_a/E_c$ (J mol <sup>-1</sup> )	100,000/160,000
Concentration Loss [6,26]	
Electrode pore radius, $\bar{r}_p$ (m)	$5 \times 10^{-7}$
Electrode porosity, $\varepsilon$ /tortuosity, $\xi$	0.5/5.9

it is cited in numerous studies and the material and geometric properties are available to conduct the modeling study as well as performing validation. Tables 2 and 3 show the model input parameters and input conditions, respectively. Table 4 provides a comparison of the present study with operation and previous simulation data. The present simulation results matched very closely with the simulation results published by Doherty et al. [6] but differs from the experimental plant data due to the simplified assumptions in this study. Nevertheless, the error associated with the current density ( $j$ ) and gross AC efficiencies are 1.14% and 3.34%, respectively, compared to the operation conditions.

### 4. Model results

#### 4.1. Setting the ATR inlet air temperature

The ATR air inlet temperature was varied from 350 °C to 550 °C over a H<sub>2</sub>O/C ratio range of 0.1–1.0, to determine the optimal inlet air temperature. These simulations were conducted at three reformer operating temperatures e.g. 700 °C, 750 °C and 800 °C. Figs. 3 and 4 show the effect of ATR air inlet temperature at a representative ATR operating temperature of 750 °C. With increasing reformer air inlet temperature the O<sub>2</sub>/C ratio decreased

**Table 3**  
Model input conditions for tubular SOFC based system validation [5,6,27].

Fuel composition, (% vol.)	CH <sub>4</sub> 81.3, C <sub>2</sub> H <sub>6</sub> 2.9, C <sub>3</sub> H <sub>8</sub> 0.4, C <sub>4</sub> H <sub>10</sub> 0.2, N <sub>2</sub> 14.3, CO <sub>2</sub> 0.9
Operating pressure ( $P_{SOFC}$ )/Ejector pressure ratio	109,431/3
Active area, (m <sup>2</sup> )	96.0768 (1152 cells)
Cell operating temperature, $T_{op}$ (°C)	910
Inlet fuel temperature, (°C)	200
Inlet air temperature, (°C)	630
H <sub>2</sub> O/C	1.8
Air utilization factor, $U_a$	0.19
Fuel utilization factor, $U_f$	0.85
Ejector fresh fuel pressure ratio	3.0
Temperature difference between the outlet of cold and hot stream of HEATX, (°C)	10
Power Output DC, $P_{el,DC}$ (kW)	120
DC to AC inverter efficiency, (%)	92
Pressure drops inside the SOFC, (bar)	0
SOFC thermal loss, (%)	2

**Table 4**

Model results compared to literature.

	Operation data [5,23,27,28]	Simulation data [6]	Present model
Voltage, (V)	nr	0.683	0.686
Current density, ( $\text{mA cm}^{-2}$ )	180	182.86	182.06
Pre-reforming temperature, ( $^{\circ}\text{C}$ )	550	535.1	535
Pre-reformer CH <sub>4</sub> conversion, (%)	10–15	25	25
Cathode inlet temperature, ( $^{\circ}\text{C}$ )	nr	823.7	826
Combustion products temperature, ( $^{\circ}\text{C}$ )	nr	1012.3	1016
Stack exhaust temperature, ( $^{\circ}\text{C}$ )	847	833.7	836
Anode inlet gas composition, (mole %)	nr	H <sub>2</sub> 26.9, CO 5.6, CH <sub>4</sub> 10.4, H <sub>2</sub> O 27.7, CO <sub>2</sub> 23.1, N <sub>2</sub> 6.2	H <sub>2</sub> 26.9, CO 5.6, CH <sub>4</sub> 10.4, H <sub>2</sub> O 27.7, CO <sub>2</sub> 23.1, N <sub>2</sub> 6.2
Anode outlet gas composition, (mole %)	H <sub>2</sub> 14.0, CO 5.0, H <sub>2</sub> O 48.0, CO <sub>2</sub> 28.0, N <sub>2</sub> 5.0	H <sub>2</sub> 11.6, CO 7.4, H <sub>2</sub> O 50.9, CO <sub>2</sub> 24.9, N <sub>2</sub> 5.1	H <sub>2</sub> 11.6, CO 7.4, H <sub>2</sub> O 50.9, CO <sub>2</sub> 24.9, N <sub>2</sub> 5.1
Stack outlet gas composition, (mole %)	N <sub>2</sub> 77.0, O <sub>2</sub> 16.0, H <sub>2</sub> O 5.0, CO <sub>2</sub> 2.0	H <sub>2</sub> O 4.5, CO <sub>2</sub> 2.3, O <sub>2</sub> 15.9, N <sub>2</sub> 77.3	H <sub>2</sub> O 4.7, CO <sub>2</sub> 2.4, O <sub>2</sub> 15.6, N <sub>2</sub> 77.2
Gross AC efficiency (LHV), (%)	50	51.28	51.67
Net AC efficiency (LHV), (%)	nr	49.15	48.42

nr = not reported.

in the H<sub>2</sub>O/C ratio range of 0.1–1.0. This was a result of the ATR air conveying more thermal energy into the reformer subsequently requiring less oxygen for adiabatic operation, and thus lowering fuel dilution by N<sub>2</sub>. At higher ATR air inlet temperature less oxygen is required by the reformer, reducing direct oxidation of H<sub>2</sub> and CO (results not reported). Based upon these observations the reformer inlet air temperature of 550 °C is chosen to reduce the number of simulations associated with the system.

#### 4.2. Effect of H<sub>2</sub>O/C on ATR product gas composition

Reforming higher hydrocarbons requires preventing of coke formation to avoid the blockage of catalyst pores and reaction active sites that may eventually make the reformer inoperative. The anode recycle also contains CO<sub>2</sub>, CO and H<sub>2</sub>, as modeled by Eq. (30)–(33).

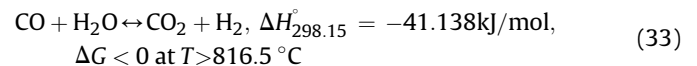
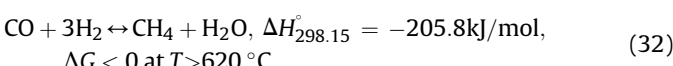
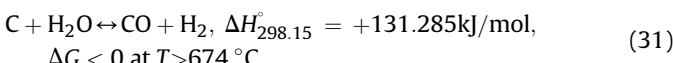
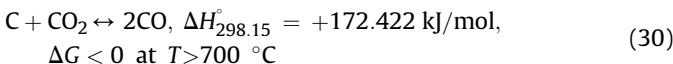


Fig. 5 shows the effect of H<sub>2</sub>O/C ratio on the reformer outlet gas composition at a representative reformer temperature of 700 °C. The O<sub>2</sub>/C ratio quickly reached a maximum value at H<sub>2</sub>O/C ratio of 0.4, followed by a steady decline with higher H<sub>2</sub>O/C ratios. At low H<sub>2</sub>O/C ratios, the reformer required more oxygen to provide the energy necessary for adiabatic operation. However, as the H<sub>2</sub>O/C ratio increased, anode recycle also increased, reducing the reformer oxygen requirement.

Increased H<sub>2</sub>O/C ratio requires higher anode recycle fraction bringing more steam and CO<sub>2</sub> into the reformer taking part in the reverse Boudouard reaction (Eq. (30)) and carbon steam reforming reaction (Eq. (31)) which are thermodynamically favorable at this temperature range. As a result, solid carbon (in the form of graphite) formation, C(gr) decreases rapidly with H<sub>2</sub>O/C ratio shown in Fig. 5. The reverse methanation reaction (Eq. (32)) also becomes thermodynamically favorable at temperatures greater than 620 °C and helped suppress methane formation with H<sub>2</sub>O/C ratio. CO/C ratio reached a peak value of 1.046 with increasing H<sub>2</sub>O/C due to the favorability of reverse Boudouard reaction, carbon steam reforming reaction, and reverse methanation reactions in the coke formation region. Solid carbon may also take part in the direct oxidation reaction in the presence of oxygen and thus can produce more CO. The H<sub>2</sub>O/C ratio at which solid carbon formation becomes

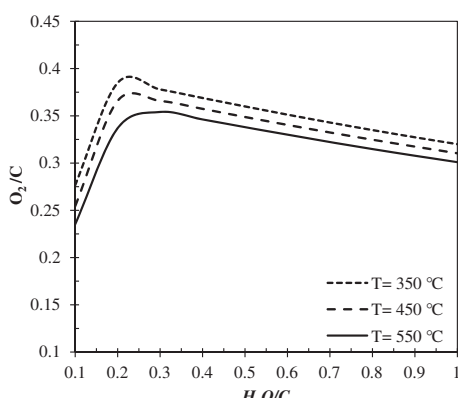


Fig. 3. Effect of ATR air inlet temperature on the O<sub>2</sub>/C.

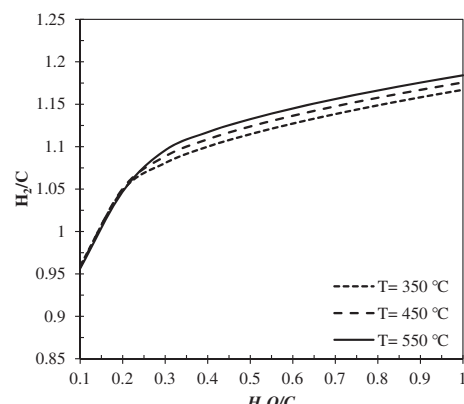
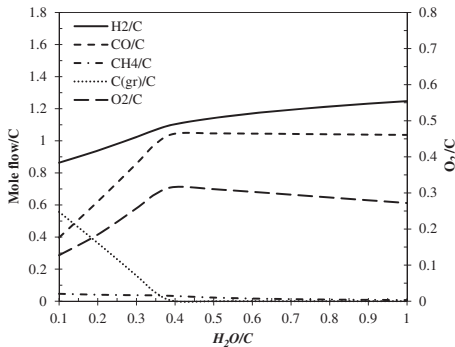


Fig. 4. Effect of ATR air inlet temperature on H<sub>2</sub>/C ratio.



**Fig. 5.** Mole flow/C at the ATR outlet stream for tubular SOFC system at  $T_{ref} = 700\text{ }^{\circ}\text{C}$ .

thermodynamically unfavorable is the minimum  $H_2O/C$  ratio above which the system should operate.

$H_2$  production increases with  $H_2O/C$  ratio due to the occurrence of more reforming reactions with the JP-8 fuel and WGS reaction (Eq. (33)). But the rate of  $H_2$  production was not strongly dependent upon the WGS reaction due to its weak thermodynamic favorability at this elevated temperature. This resulted in marginal CO decrease in the coke-free region. Some  $H_2$  may have also been oxidized due to the presence of oxygen in the ATR, producing steam.

#### 4.3. Effect of ATR temperature

ATR performance was quantified at four operating temperatures: 700 °C, 750 °C, 800 °C, and 850 °C. Solid carbon formation reduces substantially with increasing ATR operating temperature due to the high thermal decomposition of the JP-8 fuel and the high probability of the reverse Boudouard and carbon steam reforming reactions shown in Fig. 6. Favorability of reverse methanation reaction in the presence of higher  $H_2O/C$  ratio also prevents direct thermal cracking of methane thus reducing coke deposition. The minimum  $H_2O/C$  ratio to avoid any coke formation calculated are 0.4, 0.25, 0.15 and 0.12 for ATR operating temperatures of 700 °C, 750 °C, 800 °C, and 850 °C, respectively. Production of  $H_2$  decreases with temperature while production of CO increases shown in Figs. 7 and 8. At higher temperatures, the WGS reaction weakens and becomes thermodynamically unfavorable at 816 °C. Also, the anode recycle contains substantial amount of  $CO_2$  which promotes reverse WGS reaction at high temperatures to produce additional CO. Additionally, direct oxidation of  $H_2$  to steam at high temperatures might have been another cause for lower  $H_2$  production.

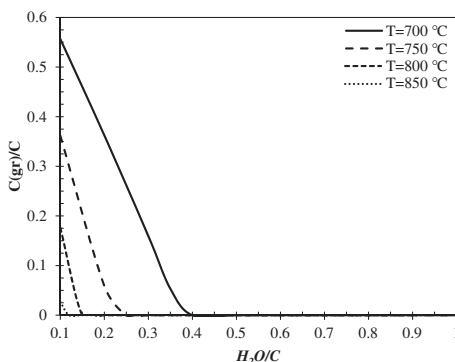


**Fig. 6.**  $C(gr)/C$  at different ATR operating temperatures.

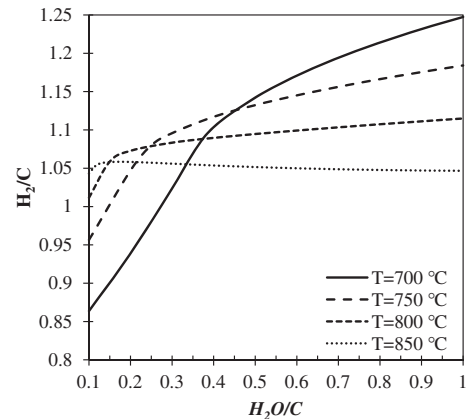


**Fig. 7.**  $H_2/C$  ratio at different ATR operating temperatures.

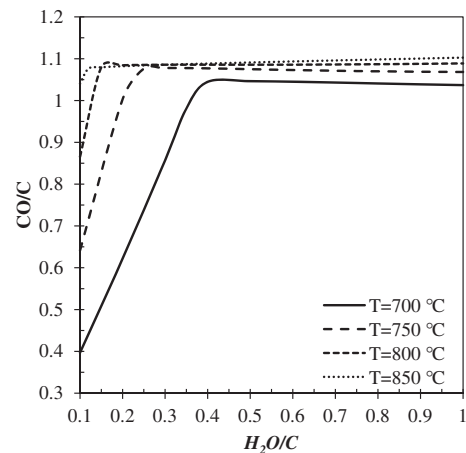


**Fig. 8.**  $CO/C$  at different ATR operating temperatures.

#### 4.4. Performance of the SOFC system

The performance of the modeled tubular SOFC based system maintained at a constant temperature of 910 °C was investigated at  $U_a = 0.167$  and  $U_f = 0.85$  in the coke-free region. Results presented in Fig. 9 shows that cell voltage decreased with  $H_2O/C$  ratio, possibly due to the decrease of  $H_2$  and CO concentrations at the anode outlet stream. Higher  $H_2O/C$  ratios required a higher anode recycle split fraction (volume basis) to meet the steam and energy

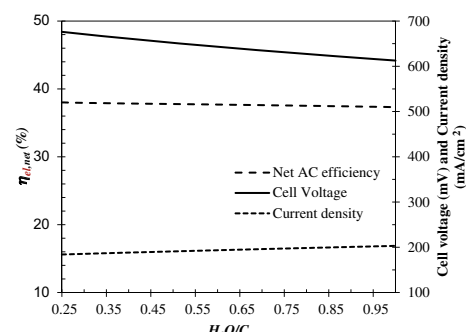


**Fig. 9.** Effect of  $H_2O/C$  ratio on the voltage, current density and net AC efficiency at  $T_{ref} = 750\text{ }^{\circ}\text{C}$ .

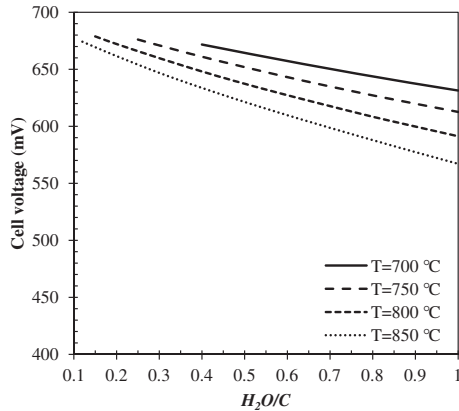


Fig. 10. Cell voltages at different ATR operating temperatures.

requirements of the reformer. Additional steam from the anode recycle led to higher  $H_2$  production through greater shifting, but the overall concentrations of  $H_2$  and CO gradually decreased due to the high volumetric flow rate of recycle stream, causing a decay in Nernst cell voltage. Current density increased proportionately with lower voltage and with  $H_2O/C$  ratio, while the ohmic, activation and concentration losses increased gradually as well. The cathode air flow rate increased to provide more oxygen in order to support the electrochemical reactions at the SOFC stack. The net AC efficiency decreased due to the higher parasitic power required by the cathode air compressor to provide this additional air requirement.

The  $H_2$  and CO concentrations at the ATR outlet stream/SOFC inlet stream were lower at higher ATR temperatures as discussed in the previous sections, thus reducing cell voltage as shown in Fig. 10. Increasing ATR temperature raised the average temperature of the SOFC streams thus lowering Gibb's energy and the resulting Nernst cell voltage. Nevertheless, the system showed the highest cell voltage of 671.7 mV at 700 °C ATR operating temperature and  $H_2O/C = 0.4$  and the lowest cell voltage of 567.1 mV at 850 °C ATR operating temperature and  $H_2O/C = 1.0$ . As shown in Fig. 11, net AC efficiency decreased with ATR operation temperature due to parasitic loss associated with higher ATR and cathode inlet air flow rates and higher fuel flow rate (not presented) required to achieve the specified power output.

Fig. 12 presents the total efficiency (summation of net AC efficiency and thermal efficiency) of the system at different ATR

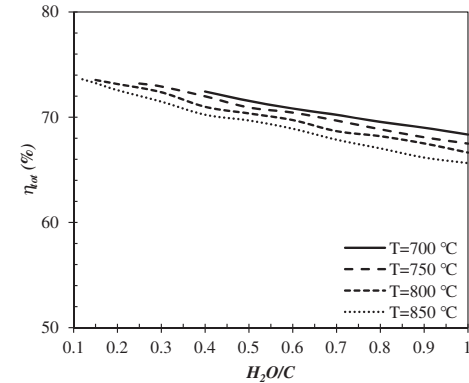


Fig. 12. Total efficiency at different ATR operating temperatures.

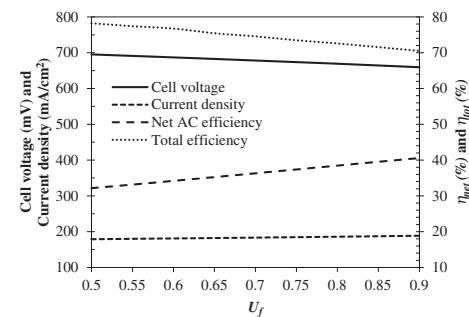


Fig. 13. Effect of  $U_f$  on voltage, efficiency and current density at  $T_{ref} = 700$  °C and  $H_2O/C = 0.5$ .

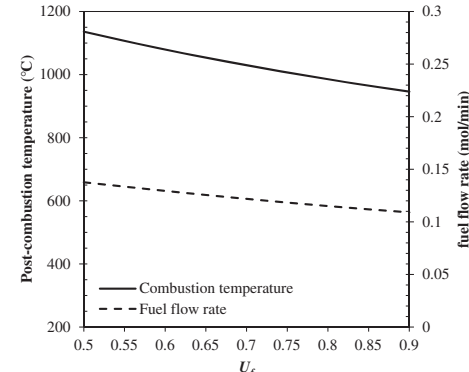


Fig. 14. Effect  $U_f$  on post combustion temperature and JP-8 flow rate at  $T_{ref} = 700$  °C and  $H_2O/C = 0.5$ .

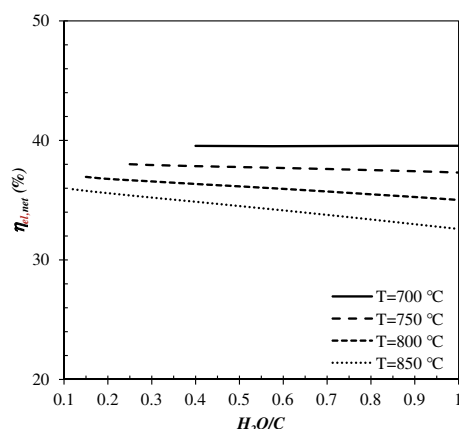
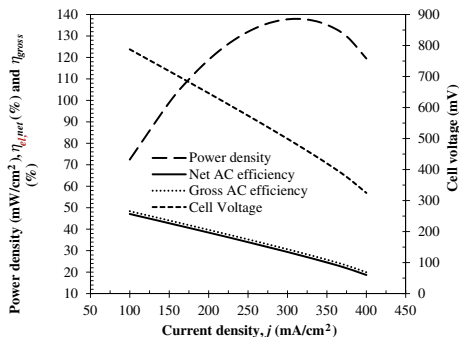


Fig. 11. Variation of net AC efficiency at different ATR operating temperatures.

operating temperatures. The thermal efficiency has been calculated keeping the temperature of the exhaust (stream-11) at 450 °C. It is assumed that the remaining exhaust heat can be used to vaporize the fresh fuel. Total efficiency was higher at lower  $H_2O/C$  ratio due to higher thermal efficiency attributed by availability of more unburned  $H_2$  and CO at the anode exhaust stream.

#### 4.5. Sensitivity analysis of the 5 kW<sub>e</sub> system

Sensitivity analyses were performed for the 5 kW<sub>e</sub> system at the highest and lowest ATR temperatures to show the influence of fuel utilization factor,  $U_f$  and the current density,  $j$  in the coke-free regions. 700 °C and 850 °C ATR operating temperatures were selected for analysis as the system demonstrated highest and



**Fig. 15.** Effect of current density on power density, efficiency and voltage at  $T_{\text{ref}} = 700 \text{ }^{\circ}\text{C}$  and  $\text{H}_2\text{O}/\text{C} = 0.5$ .

lowest net AC efficiency, respectively at these temperatures.  $\text{H}_2\text{O}/\text{C}$  ratios of 0.5 and 0.3 were maintained corresponding to the ATR operation temperatures of  $700 \text{ }^{\circ}\text{C}$  and  $850 \text{ }^{\circ}\text{C}$ , respectively. These  $\text{H}_2\text{O}/\text{C}$  ratios are slightly greater than the minimum  $\text{H}_2\text{O}/\text{C}$  ratio required to prevent coke formation in the maximum efficiency zone. The air utilization factor,  $U_a$  was kept constant at 0.167 by varying the air flow rate.

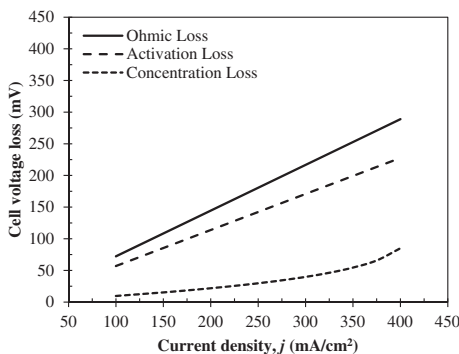


**Fig. 16.** Effect of current density on cell voltage loss at  $T_{\text{ref}} = 700 \text{ }^{\circ}\text{C}$  and  $\text{H}_2\text{O}/\text{C} = 0.5$ .

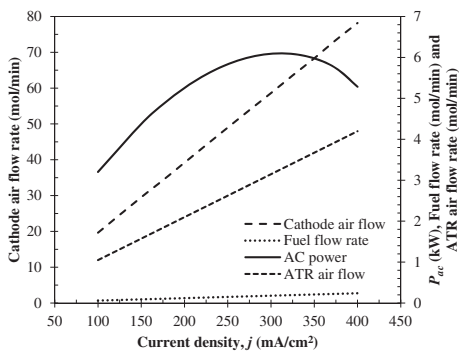


**Fig. 17.** Effect of current density on stack AC power, air flow rate and fuel flow rate of the system at  $T_{\text{ref}} = 700 \text{ }^{\circ}\text{C}$  and  $\text{H}_2\text{O}/\text{C} = 0.5$ .

**Table 5**  
Recommended operating current density,  $j$  for the systems.

$T_{\text{ref}}$ (°C)	$\text{H}_2\text{O}/\text{C}$	$j$ (mA cm $^{-2}$ )	Cell voltage (V)	$\eta_{\text{el\_net}}$ (%)	$P_{\text{ac}}$ (kW)	Power density (mW cm $^{-2}$ )
700	0.5	175–225	0.68–0.6	40.6–36.2	4.85–5.58	109.8–126.3
850	0.3		0.67–0.6	36.6–32.6	4.78–5.48	108.1–124.1

#### 4.5.1. Fuel utilization factor, $U_f$

Data presented in Fig. 13 indicates that cell voltage decreased slightly due to reduced  $\text{H}_2$  content at the anode outlet stream and more anode polarization loss. Current density increased with  $U_f$  as more  $\text{H}_2$  was consumed ( $I = 2F \times n\text{H}_2\text{,consumed}$ ) at the cells with higher  $U_f$ . The ohmic, activation and concentration losses are proportional to the current density causing a higher voltage loss with higher  $U_f$ . At low utilization factors more unburned  $\text{H}_2$  and CO go into the post combustor and release more chemical energy in the form of heat, increasing the thermal efficiency of the system. This causes a large temperature increase at the post combustor outlet, shown in Fig. 14. The high post combustion temperature increased the cathode inlet air temperature, which decreased the available Gibb's free energy and thus reduced Nernst voltage. The net AC efficiency increased as it is proportional to both  $U_f$  and cell voltage. Increasing the fuel utilization factor implies more  $\text{H}_2$  would be consumed by the SOFC stack and therefore converting more chemical energy into electrical energy, requiring less fresh JP-8 fuel, as shown in Fig. 14.

#### 4.5.2. Current density, $j$

Fig. 15 demonstrates the effect of current density on cell voltage, power density, gross and net AC efficiencies. It is observed that both voltage and efficiency decreased with current density while power density increased. As shown in Fig. 16, cell voltage decreased significantly with current density because of higher voltage losses that are directly proportional to  $j$ . The concentration loss increased sharply at higher current densities due to the inability of gaseous species to diffuse rapidly through the porous electrodes at these high current densities. Ohmic loss was dominant in the tubular SOFC based system due to the long current path of electron travel around the tubular cells. The systems showed consistent results at other ATR operating temperatures as well.

The net AC efficiency of the system decreased due to the parasitic loss associated with the compression of cathode and oxidant air streams whose flow increased with current density shown in Fig. 17. In this analysis, fuel flow rate increased at higher current density, which also lowered the system efficiency. Power density increased to a peak value of  $137.8 \text{ mW cm}^{-2}$  and  $134.7 \text{ mW cm}^{-2}$  at a current density of  $300 \text{ mA cm}^{-2}$  for ATR operating temperatures of  $700 \text{ }^{\circ}\text{C}$  and  $850 \text{ }^{\circ}\text{C}$ , respectively. In terms of efficiency, the data indicates that it was beneficial to operate the cells at lower current densities to achieve higher efficiency, thus reducing operating cost and lowering power production. So to obtain the desired power, an actual system will require more cells making the system relatively larger and more capital cost intensive. On the other hand, operating an actual system at higher current densities would require less number of cells, making the system less expensive but efficiency will be lower causing higher operating cost. A trade-off between operating cost and capital cost based on voltage, efficiency and power needs to be conducted to set the system at an optimum operating point. Table 5 shows recommended operating conditions based on this study.

## 5. Conclusion

A desulfurized JP-8 fuel based 5 kW<sub>e</sub> SOFC power unit has been modeled in this study making reference to the performance of tubular cells developed by SPGI. Results indicated that characterization of the ATR is a critical step in system evaluation, as SOFC stack performance will be largely dependent upon its operation. Further, H<sub>2</sub>O/C ratio is another key system operating parameter, because it governs coke formation and H<sub>2</sub> production. This study found a minimum H<sub>2</sub>O/C ratio of 0.4, 0.25, 0.15, and 0.12 needs to be maintained for coke-free reforming at ATR operating temperatures of 700 °C, 750 °C, 800 °C and 850 °C, respectively. But increasing H<sub>2</sub>O/C ratio causes fuel dilution which reduces the cell voltage and net system efficiency. Superior system performance has been observed at lower ATR operating temperature and lower H<sub>2</sub>O/C ratio in the coke-free region. The system demonstrated a maximum efficiency of 39.5% at 700 °C ATR operating temperature and H<sub>2</sub>O/C = 0.4 and minimum of 35.9% at 850 °C ATR operating temperature and H<sub>2</sub>O/C = 0.12 in the lower H<sub>2</sub>O/C zone. In the higher H<sub>2</sub>O/C ratio zone the maximum net AC efficiency of the system has always been observed at H<sub>2</sub>O/C = 1.0 which was 39.5% and 32.6% at 700 °C and 850 °C ATR temperatures, respectively. The system demonstrated a maximum total efficiency of 72.4% at 700 °C ATR operating temperature with H<sub>2</sub>O/C ratio of 0.4 and minimum of 65.6% at 850 °C ATR operating temperature with H<sub>2</sub>O/C ratio of 1.0.

Fuel utilization is another key parameter identified through this study. The parametric analyses showed the cell voltage marginally decreases with  $U_f$  but an increase in net AC efficiency was observed. Total efficiency decreases with  $U_f$  primarily due to reduction of thermal efficiency. Greater power density can be achieved with higher current density operation but at the expense of cell voltage and net AC efficiency. The system showed a maximum efficiency of 40.6–36.2% and 36.6–32.6% at the current density range of 175–225 mA cm<sup>-2</sup> and ATR operating temperatures of 700 °C and 850 °C, respectively, corresponding to H<sub>2</sub>O/C ratio of 0.5 and 0.3, respectively.

## Acknowledgments

The authors would like to acknowledge and thank Ohio Coal Research Center (OCRC) for their funding support and logistical assistance that made this research possible.

## References

- [1] A.S. Patil, T.G. Dubois, N. Sifer, E. Bostic, K. Gardner, M. Quah, C. Bolton, *J. Power Sources* 136 (2004) 220–225.
- [2] J.D. Stangl, R.O. Wertz, F.H. Holcomb, Military Requirements of JP-8 Fuel Reformers and Solid Oxide Fuel Cell Power Systems, Engineering Research and Development Center-Construction Engineering Research Lab, 2005, ERDC/CERL TR-05-36.
- [3] N. Lutsey, C.J. Brodrick, D. Sperling, H.A. Dwyer, *J. Transport. Res. Board* 3443 (2003) 118–126.
- [4] M. Santarelli, M. Cabrera, M. Calì, *J. Fuel Cell Sci. Technol.* 7 (2010) 021006–021011.
- [5] W. Zhang, E. Croiset, P.L. Douglas, M.W. Fowler, E. Entchev, *Energy Convers. Manage.* 46 (2005) 181–196.
- [6] W. Doherty, A. Reynolds, D. Kennedy, *Energy* 35 (2010) 4545–4555.
- [7] P. Kuchonthara, S. Bhattacharya, A. Tsutsumi, *Fuel* 84 (2005) 1019–1021.
- [8] K.D. Panopoulos, L.E. Fryda, J. Karl, S. Poulou, E. Kakaras, *J. Power Sources* 159 (2006) 570–585.
- [9] R. Suwanwarangkul, E. Croisel, M.D. Pritzker, M.W. Fowler, P.L. Douglas, E. Entchev, *J. Power Sources* 166 (2007) 386–399.
- [10] J. Sadhukhan, Y. Zhao, N. Shah, N.P. Brandon, *Chem. Eng. Sci.* 65 (2010) 1942–1954.
- [11] F. Baratto, U.M. Diwekar, D. Manca, *J. Power Sources* 139 (2004) 205–213.
- [12] S. Roychoudhury, M. Lyubovsky, D. Walsh, D. Chu, E. Kallio, *J. Power Sources* 160 (2006) 510–513.
- [13] S. Campanari, *J. Power Sources* 92 (2001) 26–34.
- [14] S. Ahmed, M. Krumpelt, *Int. J. Hydrogen Energy* 26 (2001) 291–301.
- [15] T.W. Song, J.L. Sohn, J.H. Kim, T.S. Kim, S.T. Ro, K. Suzuki, *J. Power Sources* 142 (2005) 30–42.
- [16] S.H. Chan, K.A. Khor, Z.T. Xia, *J. Power Sources* 93 (2001) 130–214.
- [17] E. Achenbach, *J. Power Sources* 49 (1994) 333–348.
- [18] E.N. Fuller, P.D. Schettler, J.C. Giddings, *Ind. Eng. Chem.* 58 (5) (1966) 19–27.
- [19] Toxicological Profile Information Sheet, Agency for Toxic Substances and Disease Registry, Georgia, 2011, Available at: <<http://www.atsdr.cdc.gov/toxprofiles/tp121-c3.pdf>> (accessed May 11, 2011).
- [20] D. Liu, T.D. Kaun, H. Liao, S. Ahmed, *Int. J. Hydrogen Energy* 29 (2004) 1035–1046.
- [21] M. Gariglio, F. De Benedictis, M. Calì, M. Santarelli, G. Orsello, *Int. J. Hydrogen Energy* 34 (2009) 4661–4668.
- [22] S. Campanari, P. Iora, *J. Power Sources* 132 (2004) 113–126.
- [23] S.E. Veyo, The Westinghouse solid oxide fuel cell program—a status report, in: IEEE Proc. 31st IECEC, vol. 2 (96570), 1996, pp. 1138–1143.
- [24] N.F. Bessette II, W.J. Wepfer, J. Winnick, *J. Electrochem. Soc.* 142 (11) (1995) 3792–3800.
- [25] P. Hofmann, K.D. Panopoulos, L.E. Fryda, E. Kakaras, *Energy* 34 (2009) 2151–2157.
- [26] F. Calise, M.D. d'Accademia, A. Palombo, L. Vanoli, *J. Fuel Cell Sci. Technol.* 5 (2008) 021014–021015.
- [27] S.E. Veyo, C.A. Forbes, in: Proceedings of the Third European Solid Oxide Fuel Cell Forum, 1998, pp. 79–86.
- [28] S. E. Veyo, W. Lundburg, in: Int. Gas Turbine and Aeroengine Congress and Exhibition, ASME-99-GT-365, Indianapolis, USA, 1999.